Performance of the CAT-TPC based on two-dimensional readout strips

Li-Sheng Yang[1] · Jin-Yan Xu[1] · Qi-Te Li[1] · Bin-Fei Ji[1] · Zi-Wei Cai[1] ·
Jia-Xing Han[1] · Shi-Wei Bai[1] · Yan-Lin Ye[1] · Xiao-Fei Yang[1] · Chen-Gui Lu[2] ·
Ning-Tao Zhang[2] · Xiao-Dong Tang[2] · Jian Gao[1] · Hong-Yi Wu[1] ·
Zhong Liu[2]

Abstract A gas detector $140 \times 140 \times 140$ mm^3 in size, termed the compact active target time projection chamber (CAT-TPC), was developed in this study to measure resonant scattering associated with cluster structures in unstable nuclei. The CAT-TPC consists of an electronic field cage, double-thick gas-electron-multiplier foils, a general-purpose digital data acquisition system, and a newly developed two-dimensional strip-readout structure. The CAT-TPC was operated using a ^{4}He (96%) + CO$_2$ (4%) gas mixture at 400 mbar. The working gas also serves as an active target for tracking charged particles. The overall performance of the CAT-TPC was evaluated using a collimated α-particle source. A time resolution of less than 20 ns and a position resolution of less than 0.2 mm were observed along the electron drift direction. Three-dimensional images of incident trajectories and scattering events can be clearly reconstructed under an angular resolution of approximately 0.45 degree.

Keywords AT-TPC · Readout strips · Guard ring · Three-dimensional image

✉ Qi-Te Li
liqt@pku.edu.cn

[1] School of Physics and State Key Laboratory of Nuclear Physics and Technology, Peking University, Beijing 100871, China

[2] Institute of Modern Physics, Chinese Academy of Sciences, Lanzhou 730000, China

1 Introduction

The time projection chamber (TPC) is a type of gas detector possessing excellent imaging capabilities [1]. It yields good space-time resolution, high detection efficiency, and almost 4π solid-angle coverage. Owing to these advantages, it has been widely used in high-energy physics experiments for several decades [2–8]. In recent years, with the development of research in nuclear physics involving the usage of radioactive ion beams (RIB), the TPC has also gradually been applied in low-energy nuclear physics experiments, with some relevant modifications [9–14].

Because the beam intensity of RIBs is typically low, a thick target is often used to mitigate this constraint. However, a thick target limits the momentum resolution and acceptance of the detector; therefore, a difficult compromise must be made between the target thickness and resolution. Active target TPCs (AT-TPCs), in which the reaction target also serves as the detection material, serve as a good solution here. These can determine the location of the reaction vertex and the tracks of the ions emitted from the reaction, along with the associated energy loss inside the gas volume. This enables the use of a thick target to increase the reaction yield while retaining good resolution and acceptance at each reaction location [15, 16]. For instance, a prototype AT-TPC, designed by NSCL and applying micromegas amplification technology, involves a large active volume and detects the α cluster structure in ^{14}C through resonant scattering [17]. Recently, the MAIKo detector, designed by Kyoto University and applied μ-PIC

for electron amplification and two-dimensional readout, was successfully applied to observe the 3α breakup events from the Hoyle state in ^{12}C [18]. The latest progress has also been covered in a review article [19].

Clustering in the light mass region is of special importance for understanding the exotic nuclear structure as well as nucleosynthesis in cosmos. For nearly five decades, clear experimental evidence on nuclear clustering has been accumulated, but several unknowns remain, particularly in the case of unstable nuclei [20]. For studies on unstable nuclei using RIBs, the AT-TPC has the advantage of recording the complete kinematic information under a relatively low beam intensity, which is particularly useful for cluster-structure studies by using resonant scattering on the helium target [21, 22]. The requirement for the resolution of the reconstructed energy spectrum is approximately 50–100 keV [19]. Our research group is also interested in investigating cluster structures in unstable nuclei [23, 24], for which new detection technologies such as the AT-TPC are required. In the present study, a compact AT-TPC was developed to measure the resonant scattering of clustering systems.

Previously, the first version of the AT-TPC prototype was reported, and it was equipped with one-dimensional readout strips and provided two-dimensional track images [25]. Currently, however, specially designed two-dimensional readout strips allowing for the recording of three-dimensional images have been implemented. The structure details and detection performance of this second-version prototype are reported in this article.

2 Design of the CAT-TPC

2.1 Overall description

A schematic view of the compact active target time projection chamber (CAT-TPC) is shown in Fig. 1. The CAT-TPC in this study consisted of a gas vessel, field cage, and an end-cap readout board collected in the electronic circuit. The volume of the field cage was $140 \times 140 \times 140$ mm^3. The drift field was provided by a number of 100 μm-diameter gold-plated tungsten wires, doubly wound with 10-mm spacing around the cage frame composed of a printed circuit board (PCB). The cage was installed between the cathode plate at the top and the readout board at the bottom. When a charged particle passed through the cage volume filled by the sensitive gas, the deposited energy caused gas ionization along the particle track. The electric field in the cage drove the electrons (ions) to drift toward the electrodes. The electron signals were then multiplied by a thick gas-electron-multiplier (thick GEM)
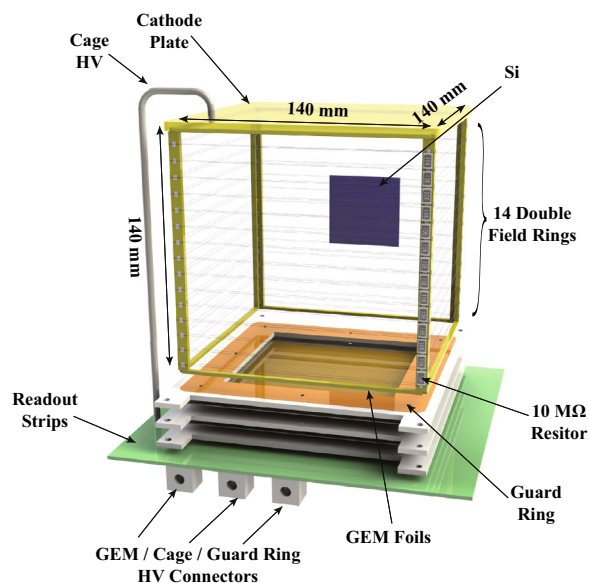

Fig. 1 (Color online) Schematic view of the CAT-TPC

foil [26]. The sensitive area of the GEM foil was only 100 $\times$ 100 mm^2, which limited the sensitive volume of the TPC to approximately $100 \times 100 \times 140$ mm^3. Details of the GEM foils are described in Sect. 2.2. The signals from the GEM foil were collected using two-dimensional copper strips printed on a PCB, as shown in Fig. 2a. Among them, 48 parallel strips were placed in the X direction, perpendicular to the other 40 parallel strips in the Y direction. The latter set of 40 strips were divided into 80 half-strips by isolating the cut at the middle (refer to Sect. 3.3 for an elaboration). To distinguish the strips, the 40 half-strips on the left side of the Y-axis were numbered using even numbers, while those on the right side were numbered using odd numbers. This two-dimensional strip-readout configuration effectively reduces the number of readout electronics while maintaining the necessary spatial resolution in the X–Y dimensions.

To describe the TPC performance, it is convenient to define a coordinate system with the Z-axis along the
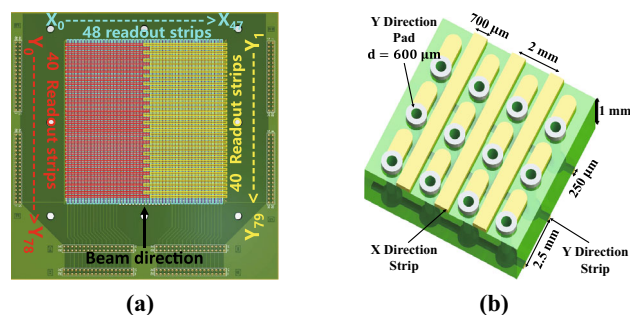

Fig. 2 (Color online) **a** Schematic view of readout PCB and **b** amplified details of X–Y readout structure

average electron drift direction in the cage, and the X–Y axes lying in the readout plane. A total of 48 parallel X-strips 700-μm in width and 48 rows of pads were positioned alternatively, as shown in Fig. 2b. Each pad was extended to the rear side of the board via a hole and collected to one of the Y-strips. In order to enhance the position resolution, each Y-strip was divided into two sections using an isolating cut near the strip-middle, as can be seen in Fig. 2a.

2.2 Thick GEM foils

Thick GEM readout is a new technique enabling signal amplification with high spatial resolution, whereby higher voltages can be withstood, and a high tolerance of PM 2.5 to air dust can be obtained [27–29]. The thick GEM adopted in this study was 200 μm in thickness, consisting of a dielectric clad on both sides of a thin copper layer, which is characterized by a high-density array of holes. When a voltage of 300–400 V was applied to the copper layer, the electron signal collected from the field cage could be amplified by two to three orders of magnitude. Two thick GEM layers, separated by 3 mm, were employed in the present design. A bias voltage of approximately 300 V was applied to each thick GEM through a custom-made circuit (Fig. 3). Notably, a gain of 10^3 can be achieved for electron multiplication via this double-thick GEM arrangement [30, 31]. In addition to thick GEM, home-made charge-sensitive preamplifiers were also used, the sensitivity of which was approximately 20 mV/MeV.
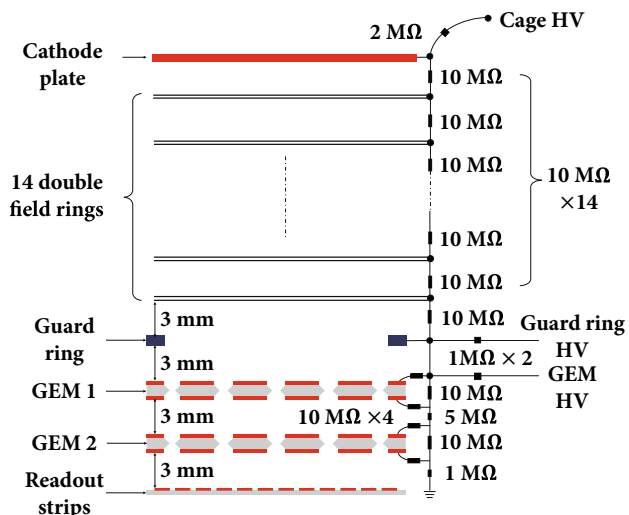
2.3 Field cage

The method to supply high voltage (HV) to the field cage is depicted in Fig. 3. The field cage provides a vertical static electric field inside its sensitive volume, with some field distortion near the edge owing to the finite range of the electrode and the wires. Based on the Garfield code simulation [32], a guard ring was applied to improve the uniformity of the drift field. The ring was located 3.0 mm above the first GEM foil (Fig. 3). The high voltage applied to the guard ring was supplied independently and could be tuned to yield the best performance. According to the test, the field intensity at the edge was sensitive to the guard ring voltage. The best field uniformity was obtained at approximately 900 V [25].

2.4 Signal processing and acquisition

As part of the experiments in this study, a ^{241}Am α-particle source was applied to generate particle tracks in the field cage (Fig. 4). The signals from the anode readout strips were sent to the PKU preamplifiers, which were connected to the data acquisition (DAQ) system. In addition to the CAT-TPC, a silicon detector with a 48 × 48 mm^2 active area was employed to provide the trigger signal.

A general-purpose digital DAQ system (GDDAQ) was used [33], which is based on the Pixie-16 module of XIA LLC [34]. The Pixie-16 processor was designed as an industry standard compact PCI/PXI module. When compared to the traditional CAMAC or VME DAQ systems, it has the advantages of a relatively high data transfer rate (up to 109 MByte/s) and enables online digital spectrometry and waveform acquisition for 16 input signals per module. Several modules can be hosted in a single crate.
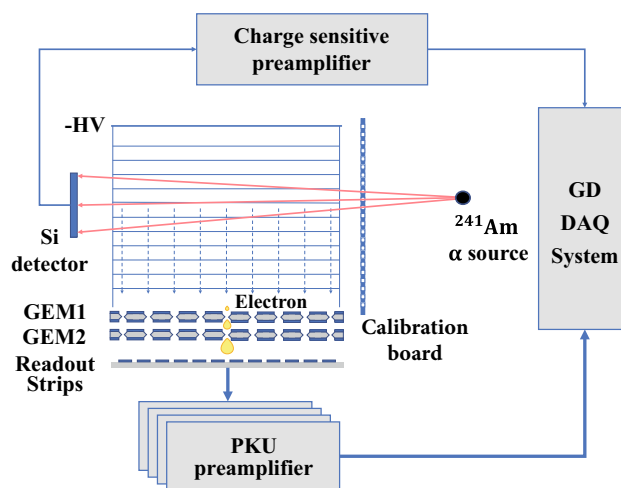

Fig. 3 (Color online) HV circuit for the field cage and the GEM foils

Fig. 4 (Color online) Readout electronics and DAQ

2.5 Working gas mixture

The CAT-TPC was installed in a sealed gas chamber filled with a gas mixture that functioned as the target material as well as the active detection medium. The main gas composition was of ^{4}He, with 4% of CO_2, which helped to stabilize the gain [18]. The gas pressure was set to 400 mbar and controlled via a floating gas pneumatic system.

3 Test measurements

3.1 Experimental setup

A schematic top view of the experimental setup is presented in Fig. 5. The entire detection system was installed in a gas chamber filled with the working gas. A calibration board was inserted between the α-particle source and CAT-TPC. A two-dimensional array of holes, each with a diameter of 2 mm and distanced by 5 mm from one another, were made on the board. Located on the other side of the CAT-TPC was an auxiliary Si detector providing the start timing signal.

Limited by the size of the Si detector, only the particles passing through an array of 3 × 3 holes can be recorded appropriately. Figure 6 demonstrates an example of the track profile in Y–Z plane (Fig. 5).

3.2 Track position determination

When a particle passes through the sensitive gas volume, the deposited energy generates ions and electrons around the track. Electrons drift towards the GEM foil along the electric field lines in the Z-direction. The recorded drift times correspond to the Z-positions of the track,
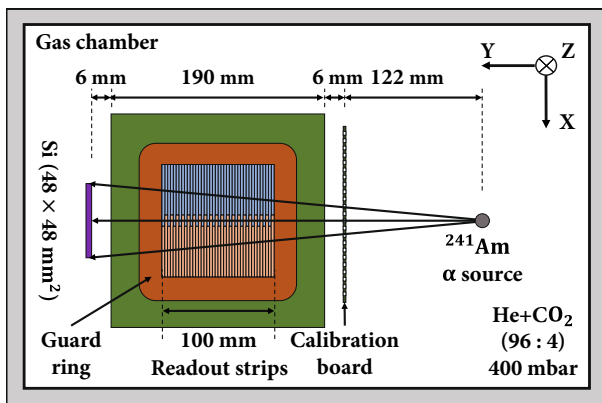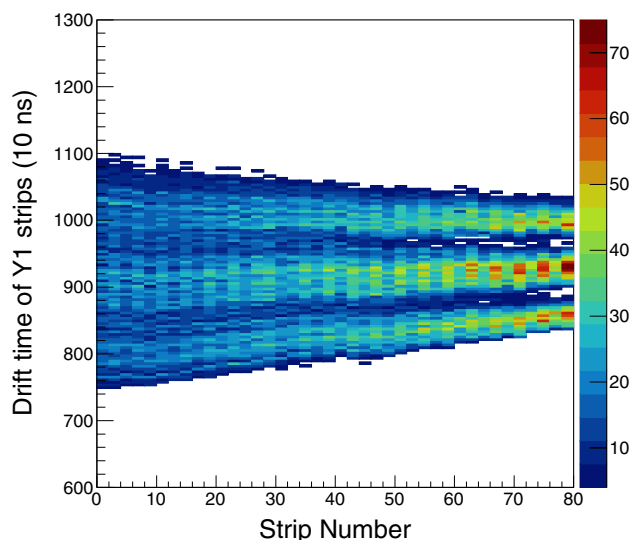

Fig. 6 (Color online) Track profile of particles passing through the holes on the calibration board and recorded by the CAT-TPC

while the crossing points of the fired X- and Y-strips yield the corresponding X- and Y-positions. This is the principal of CAT-TPC, which provides a three-dimensional image of a particle track.

First, the timing signals from various strips are matched to one another by using the correct time offset for each readout channel. This was realized herein using a pulse generator, which allows for the matched signals to be sent to all strips. After calibration of the time offset, a 3 × 3 matrix of holes may be selected on the calibration board in front of a small α-particle source (refer to Fig. 5 for the arrangement). The recorded drift-time track profiles may produce corresponding 3 × 3 centroids on the plane on the left side of the field cage. The corresponding absolute Z-positions of these centroids can be obtained by projecting straight lines between the source and calibration holes onto the left-side plane of the cage. By using these drift-time centroids and the corresponding absolute positions, the drift velocity along the Z-direction can be deduced. Using this calibration method, all drift times from each individual track can be converted into the corresponding Z-positions, as shown in Fig. 6 as an example.

During the experiment, HVs of −2150, −820 and −890 V were applied to the cage, GEM foil, and guard ring, respectively. Under this condition, drift velocities between 9.91 and 10.08 mm/μs were obtained for different readout strips, as shown in Fig. 7, which is in good agreement with the simulation results using Garfield code. This variation may be attributed to the uniformity of the electric field, determination of the centroid of the track profile, and transmission of the electric signals.

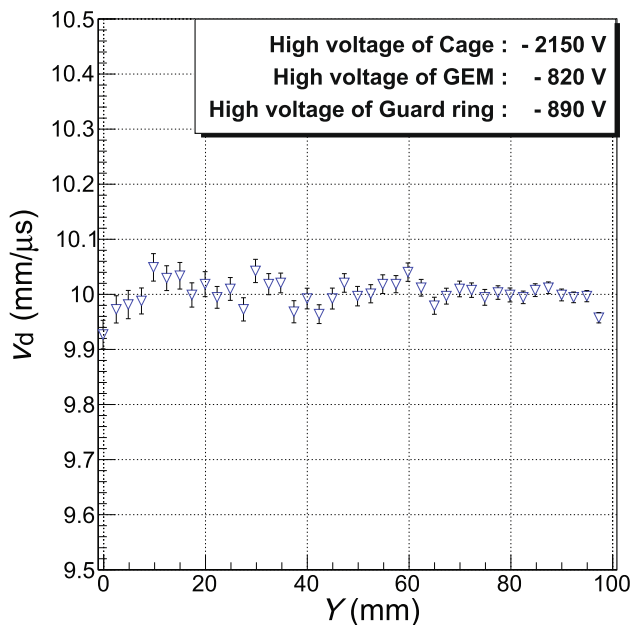The time resolution of the CAT-TPC along the Z-axis can be deduced using the residual method [25, 35]. For

Fig. 5 (Color online) Top view of the experimental setup. The reference system is indicated in the upper right corner

Fig. 7 Drift velocity as a function of Y-position

Fig. 8 (Color online) Example of a ^{4}He beam track of the anode strips

each measured track, a straight line was applied to fit the drift-time data. The residual time for the i-th readout strip is defined as:

$$t_i = T_i^{\mathrm{F}} - T_i^{\mathrm{D}}, \tag{1}$$

where T_i^{F} and T_i^{D} are the fitted and detected times, respectively. Repeated for many tracks, t_i normally forms an approximate Gaussian distribution, from which the standard deviation σ_{ti} can be extracted as the time resolution. This resolution for all Y-strips varies from 6.6 to 15.5 ns, corresponding to Z-position resolutions from 0.07 to 0.15 mm by considering the average drift velocity of approximately 10 mm/µs. The time resolution due to electronics is approximately 1.9–4.6 ns, depending on the readout strip, which is relatively small.

The spatial resolution in the X or Y directions for the readout board is modulated by the period of the readout strips and can be estimated as $\sigma_X = 2 \text{ (mm)}/\sqrt{12} = 0.58$ (mm), $\sigma_Y = 2.5 \text{ (mm)}/\sqrt{12} = 0.72$ (mm) [36], where 2 mm and 2.5 mm are the strip pitches along the X and Y directions, respectively. A more realistic X-Y plane resolution is analyzed in Sect. 3.3.

Based on the performance of spatial resolution, the track angular resolution along the Z direction can be estimated. Each measured particle track can be divided into two sections: the upstream and downstream ones. Each section contains data from 20 readout strips that can be fitted by a straight line. The trajectory angles for the two sections are denoted as θ_{up} and θ_{down} [18], respectively, as indicated in Fig. 8. The difference between these two angles, $\theta_{\mathrm{up}} - \theta_{\mathrm{down}}$, can be accumulated for many tracks. The
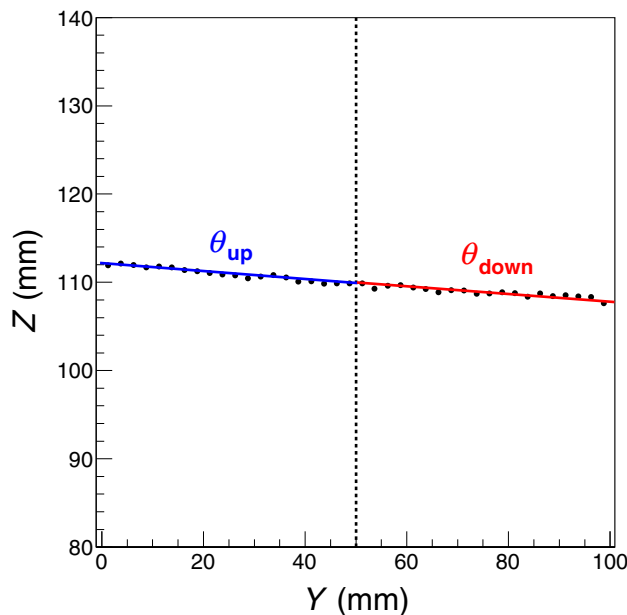
distribution thereof became a Gaussian-type spectrum, from which a standard deviation of $\sigma_{\mathrm{up\text{-}down}} = 0.39 \pm 0.01$ degree was extracted for the present measurement. The track angular resolution was approximately $\sigma_{\mathrm{track}} = \sigma_{\mathrm{up\text{-}down}}/\sqrt{2} = 0.28$ degree [18].

3.3 3-D tracking reconstruction

Using the recorded X–Z and Y–Z information for each track, we could reconstruct its 3-dimensional pattern. We adopted the following algorithm:

(1) Fit all data points in X–Z plane by a two-dimensional straight-line to obtain the function $Z = f(X)$ and its inverse function $X = g(Z)$;
(2) For each (Y_i, Z_i) point, find an associated $X_i = g(Z_i)$.
(3) Collect all (X_i, Y_i, Z_i) to form a 3-dimensional track.

Obviously, the above process may be started from the $Y - Z$ plane as well. In the case of scattering or reaction, two trajectories may appear following the interaction point (vertex). This point is related to a sudden change in signal amplitude. An example of the detected α-He scattering event is shown in Fig. 9 as an example. In Sect. 2.1, we provide a description of the readout Y-strips, which are divided into two sections of half-strips (Fig. 2a). The reason for adopting this complexity is mainly to obtain better two-track discrimination. As shown in Fig. 9, when two tracks appear after a scattering or reaction, each associated Y-strip should record two signals. If these two signals are too close to each other in comparison with the signal
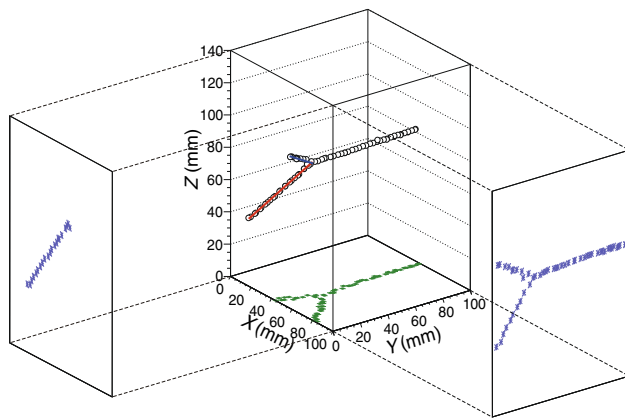
Fig. 9 (Color online) The reconstructed three-dimensional tracks for an α-He scattering event and its projection onto X–Z, Y–Z and X–Y planes

discrimination, the information for the two tracks would be lost or biased. By using the divided Y-strips, at least for an incident track near the center of the X-coordinate (middle of the Y-strip), signals for the two tracks after scattering or reaction will be separately recorded by the two strip-sections; hence, the overlap of close-by signals will not occur and the scattering (reaction) image, including that around the vertex, can be clearly reconstructed, as demonstrated in Fig. 9.

It should be noted that when a track is almost parallel to the X-Y plane and all acquired Z_i-positions have similar values, $X_i = g(Z_i)$ conversion has no unique result, and the above method is no longer valid. In this case, we may simply allocate the two-end values of the X-strips to the track-start and -stop positions, with the former being related to the particle incident (or scattering vertex) X-position. The other X-positions can then be deduced according to linear interpolations.

The position of each track on the X–Y plane can be reconstructed using the algorithm described above. Similar to the aforementioned residual analysis method [25, 35] for the Z-dimension, a straight line can also be applied to fit the projected track in the X–Y plane. The distance between the measured positions and fitting line was recorded to form the residual distribution. The value of the root-mean-square of this distribution is approximately 0.70 mm, which may represent the spatial resolution in the X–Y plane. The angular resolution for a three-dimensional track can also be evaluated by applying the two-section method described above. The result from the present test measurement was approximately 0.45 degree. A similar method may also be applied to determine the closest distance between the incident and scattered tracks. The present mean value is 0.49 mm, which is consistent with the overall position resolution.

4 Summary

In this study, a newly developed two-dimensional strip readout structure was successfully applied to the CAT-TPC, along with the thick GEM foil amplification and GDDAQ. This readout structure was deployed for the three-dimensional image reconstruction of a particle track or scattering event. The Y-strips were divided into two sections such that scattering or reaction events could be reasonably recorded. The detector performance was tested using a ^{241}Am α source. A time resolution (standard deviation) of less than 16 ns and a spatial resolution of less than 0.15 mm along the Z-dimension were obtained. The uncertainty in the X- or Y-dimension was approximately 0.7 mm, according to the residual analysis. Based on the readout-strip design and the reconstruction algorithm, the scattering or reaction event can be clearly imaged under an angular resolution of approximately 0.45 degree. These performances are sufficient for this CAT-TPC to be used in low-energy nuclear physics experiments, such as in the resonant scattering experiment for cluster-structure studies.

References

1. J.N. Marx, D.R. Nygren, The time projection chamber. Phys. Today **31**(10), 46–53 (1978). https://doi.org/10.1063/1.2994775
2. P. Juyal, K.L. Giboni, X.D. Ji et al., On proportional scintillation in very large liquid xenon detectors. Nucl. Sci. Tech. **31**, 93 (2020). https://doi.org/10.1007/s41365-020-00797-4
3. K.L. Giboni, P. Juyal, E. Aprile et al., A LN_2-based cooling system for a next-generation liquid xenon dark matter detector. Nucl. Sci. Tech. **31**, 76 (2020). https://doi.org/10.1007/s41365-020-00786-7
4. H. Yang, Z.F. Xu, J. Tang et al., Spin coating of TPB film on acrylic substrate and measurement of its wavelength shifting efficiency. Nucl. Sci. Tech. **31**, 28 (2020). https://doi.org/10.1007/s41365-020-0737-5
5. C. Brand, G. Cairanti, P. Charpentier et al., The DELPHI time projection chamber. Nucl. Instrum. Methods A **283**, 567–572 (1989). https://doi.org/10.1109/23.34417
6. M. Anderson, F. Bieser, R. Bossingham et al., The STAR time projection chamber: a unique tool for studying high multiplicity events at RHIC. Nucl. Instrum. Methods A **499**, 659–678 (2003). https://doi.org/10.1016/S0168-9002(02)01964-2
7. J. Bachler, J. Bracinik, H.G. Fischer et al., Development of a TPC detector for the ALICE experiment. Nucl. Instrum. Methods A **419**, 511–514 (1998). https://doi.org/10.1016/S0168-9002(98)00858-4

8. B.J. Zheng, Y.L. Li, Z.Y. Deng et al., Drift field improvement and test in a GEM-TPC prototype. Chin. Phys. C **35**, 56–60 (2011). https://doi.org/10.1088/1674-1137/35/1/012

9. G.D. Alkhazov, M.N. Andronenko, A.V. Dobrovolsky et al., Nuclear matter distributions in ^{6}He and ^{8}He from small angle p-He scattering in inverse kinematics at intermediate energy. Phys. Rev. Lett. **78**, 2313–2316 (1997). https://doi.org/10.1103/PhysRevLett.78.2313

10. B. Blank, L. Hay, J. Huikari et al., A time projection chamber for the three-dimensional reconstruction of two-proton radioactivity events. Nucl. Instrum. Methods A **613**, 65–78 (2010). https://doi.org/10.1016/j.nima.2009.10.140

11. X.Y. Liu, Y.W. Yang, R. Liu et al., Measurement of the neutron total cross section of carbon at the Back-n white neutron beam of CSNS. Nucl. Sci. Tech. **30**, 139 (2019). https://doi.org/10.1007/s41365-019-0660-9

12. X.Y. Zhao, F. Liu, Z. Deng et al., GERO: a general SCA-based readout ASIC for micro-pattern gas detectors with configurable storage depth and on-chip digitizer. Nucl. Sci. Tech. **30**, 131 (2019). https://doi.org/10.1007/s41365-019-0659-2

13. A. Fritsch, T. Suzuki, A. Tamii et al., High-resolution study of Gamow–Teller transitions in the ^{48}Ti(^{3}He, t)^{48}V reaction. Phys. Rev. C **93**, 064326 (2016). https://doi.org/10.1103/PhysRevC.93.064326

14. D. Suzuki, M. Ford, D. Bazin et al., Prototype AT-TPC: toward a new generation active target time projection chamber for radioactive beam experiment. Nucl. Instrum. Methods A **691**, 39–54 (2012). https://doi.org/10.1016/j.nima.2012.06.050

15. M. Caamano, W. Mittig, H. Savajols et al., Resonance state in ^{7}H. Phys. Rev. Lett. **99**, 062502 (2007). https://doi.org/10.1103/PhysRevLett.99.062502

16. S. Bailey, M. Freer, S. Cruz et al., Energy levels of ^{18}F from the ^{14}N + α resonant reaction. Phys. Rev. C **90**, 024302 (2014). https://doi.org/10.1103/PhysRevC.90.024302

17. T. Ahn, D.W. Bardayan, D. Bazin et al., The prototype active-target time-projection chamber used with TwinSol radioactive-ion beams. Nucl. Instrum. Methods B **376**, 321–325 (2016). https://doi.org/10.1016/j.nimb.2015.12.042

18. T. Furuno, T. Kawabata, H.J. Ong et al., Performance test of the MAIKo active target. Nucl. Instrum. Methods A **908**, 215–224 (2018). https://doi.org/10.1016/j.nima.2018.08.042

19. D. Bazin, T. Ahn, Y. Ayyad et al., Low energy nuclear physics with active targets and time projection chambers. Progr. Part. Nucl. Phys. **114**, 103790 (2020). https://doi.org/10.1016/j.ppnp.2020.103790

20. Y. Liu, Y.L. Ye, Nuclear clustering in light neutron-rich nuclei. Nucl. Sci. Tech. **29**, 184 (2018). https://doi.org/10.1007/s41365-018-0522-x

21. D. Suzuki, T. Ahn, D. Bazin et al., Cluster structure of neutron-rich 10Be and 14C via resonant alpha scattering. Nuovo Cimento C **39**, 372 (2016). https://doi.org/10.1393/ncc/i2016-16372-0

22. W. Mittig, S. Beceiro-Novo, A. Fritsch et al., Active target detectors for studies with exotic beams: present and next future. Nucl. Instrum. Methods A **784**, 494–498 (2015). https://doi.org/10.1016/j.nima.2014.10.048

23. Z.H. Yang, Y.L. Ye, Z.H. Li et al., Observation of enhanced monopole strength and clustering in ^{12}Be. Phys. Rev. Lett. **112**, 162501 (2014). https://doi.org/10.1103/PhysRevLett.112.162501

24. Y. Liu, Y.L. Ye, J.L. Lou et al., Positive-parity linear-chain molecular band in ^{16}C. Phys. Rev. Lett. **124**, 192501 (2020). https://doi.org/10.1103/PhysRevLett.124.192501

25. J.Y. Xu, Q.T. Li, Y.L. Ye et al., Performance of a small AT-TPC prototype. Nucl. Sci. Tech. **29**, 97 (2018). https://doi.org/10.1007/s41365-018-0437-6

26. F. Sauli, New observations with the gas electron multiplier (GEM). Nucl. Instrum. Methods A **396**, 50–66 (1997). https://doi.org/10.1016/S0168-9002(97)00648-7

27. H.B. Liu, Q. Liu, S. Chen et al., A study of thinner-THGEM, with some applications. J. Instrum. **7**(06), C06001 (2012). https://doi.org/10.1088/1748-0221/7/06/C06001

28. Q. Liu, H.B. Liu, S. Chen et al., A successful application of thinner-THGEMs. J. Instrum. **8**(11), C11008 (2013). https://doi.org/10.1088/1748-0221/8/11/C11008

29. C. Shalem, R. Chechik, A. Breskin et al., Advances in thick GEM-like gaseous electron multipliers—part I: atmospheric pressure operation. Nucl. Instrum. Methods A **558**, 475–489 (2006). https://doi.org/10.1016/j.nima.2005.12.241

30. M. Cortesi, J. Yurkon, A. Stolz, Operation of a THGEM-based detector in low-pressure Helium. J. Instrum. **10**(2), P02012 (2015). https://doi.org/10.1088/1748-0221/10/02/P02012

31. M. Cortesi, S. Rost, W. Mittig et al., Multi-layer thick gas electron multiplier (M-THGEM): a new MPDG structure for high-gain operation at low-pressure. Rev. Sci. Instrum. **88**(1), 013303 (2016). https://doi.org/10.1063/1.49743331

32. Garfield-simulation of gaseous detectors. http://cern.ch/garfield

33. H.Y. Wu, Z.H. Li, H. Tan et al., A general-purpose digital data acquisition system (GDDAQ) at Peking University. Nucl. Instrum. Methods A **975**, 164200 (2020). https://doi.org/10.1016/j.nima.2020.164200

34. https://www.xia.com/DGF_Pixie-16.html

35. H.B. You, Z.H. Yang, Y.L. Ye et al., Construction and calibration of the multi-neutron correlation spectrometer at Peking University. Nucl. Instrum. Methods A **728**, 47–52 (2013). https://doi.org/10.1016/j.nima.2013.06.037

36. F. Wang, B. Nachman, M. Garcia-Sciveres, Ultimate position resolution of pixel clusters with binary readout for particle tracking. Nucl. Instrum. Methods A **899**, 10–15 (2018). https://doi.org/10.1016/j.nima.2018.04.053